

# How calcium prevents precipitation hardening in Al–Mg–Si alloys

Sigurd Wenner<sup>a</sup>, Calin D. Marioara<sup>b</sup>, Sigmund J. Andersen<sup>b</sup>, Randi Holmestad<sup>a</sup>,

<sup>a</sup>*Department of Physics, NTNU, Høgskoleringen 5, NO-7491 Trondheim, Norway*

<sup>b</sup>*Materials and Chemistry, SINTEF, Box 4760 Sluppen, NO-7465 Trondheim, Norway*

---

## Abstract

We have investigated the effect on precipitate microstructure and hardness upon adding small amounts of Ca to a base Al–Mg–Si alloy. The main investigative techniques were transmission and scanning electron microscopy. We found that large Ca-containing particles with composition  $\text{CaAl}_2\text{Si}_2$  form during the production stages of the alloy. The particles leave less Si available in solid solution for the nucleation of hardening precipitates, leading to a coarser microstructure consisting of less coherent precipitates. The resulting hardness decrease is measurable for alloys containing more than 60 at.ppm of Ca.

*Keywords:* Aluminium alloys, Calcium, Precipitation, Transmission electron microscopy, Scanning electron microscopy

---

## 1. Introduction

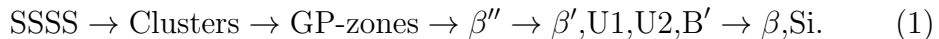
Recycled aluminium constitutes a steadily growing fraction of the global aluminium supply. In addition to avoiding disposing of scrap metal, an im-

---

*Email address:* [randi.holmestad@ntnu.no](mailto:randi.holmestad@ntnu.no) (Randi Holmestad)

portant reason for using recycled aluminium is the reduced production energy. In total, producing recycled aluminium has an energy cost of only a few percent of that of producing it from bauxite [1]. The main disadvantage of recycled material is the accidental introduction of trace elements, which can be both detrimental and beneficial for the properties of alloys.

The subject of this study is the age-hardenable *6xxx* aluminium alloy series, where the main alloying elements are magnesium and silicon. *6xxx* alloys constitute the largest share of produced aluminium alloys, and are heavily used for both architectural and automotive purposes [1]. Upon appropriate heat treatment, Mg and Si atoms cluster to form nano-sized metastable precipitates. These prevent the motion of dislocations when the material is under stress, and thus increase the strength of the material. The precipitates form in a sequence, starting with phases which are coherent with the Al matrix and ending in large, incoherent phases with the lowest bulk formation enthalpy. The precipitation sequence for the Al–Mg–Si system is [2, 3, 4]:



The metastable and fully coherent  $\beta''$  is the main hardening phase. Like all the metastable phases, it is needle-shaped and has its main growth direction along  $\langle 001 \rangle_{\text{Al}}$ .

Calcium is a common impurity element in aluminium as it can be introduced at many steps during the production [5]. In Al–Mg–Si alloys, it is known to be detrimental to their mechanical strength [1, 5], making control of the Ca content important both during primary production and recycling of alloys. A decrease in strength with Ca content signifies a change in precipitate microstructure, which is worth investigating due to the industrial

relevance of Ca additions. Calcium is located underneath magnesium in the alkaline earth metal group in the periodic table of elements, which gives reason to believe that Ca atoms can replace Mg atoms in precipitate structures characteristic of the Al–Mg–Si system. By analogy, the replacement of Si by Ge was previously investigated. Al–Mg–Ge alloys contain precipitate types related to those in Al–Mg–Si, and small additions of Ge to Al–Mg–Si alloys has been found to promote nucleation [6].

In this paper we present a study of the microstructure in Al–Mg–Si alloys with different Ca content, from trace amounts to typical alloying amounts, and explain why Ca additions reduce the mechanical strength of this class of alloys. The main characterization technique was electron microscopy in its transmission and scanning variants (TEM and SEM). Details regarding the experimental procedures are given in the next section. Results of hardness measurements, microscopy and spectroscopy are found in Sec. 3 and discussed in Sec. 4, while Sec. 5 serves as a conclusion.

## 2. Experimental

The alloys chosen for this study is a subset of alloy compositions created for the investigation of trace element influences on precipitation. Having a total solute concentration of  $\approx 1$  at.%, the base alloy is low-solute (lean) by industrial standards for *6xxx* alloys. Its commercial counterpart is 6060, which has comparable Mg and Si content. The exact compositions of the three Ca-containing alloys were measured by inductively coupled plasma optical emission spectroscopy (ICP-OES), and are given in Table 1.

The material was extruded as cylindrical rods of cross-sectional diameter

Table 1: Compositions of the samples (at.%), measured by ICP-OES.

Alloy	Mg	Si	Fe	Ca
LCa1	0.53	0.40	0.034	0.0019
LCa2	0.52	0.40	0.033	0.0060
LCa3	0.53	0.39	0.033	0.0727

20 mm. Solution heat treatment at 540 °C was carried out for 1 hour, followed by quenching in room-tempered water. The rods were cut into 10 mm long samples and stored at room temperature for 4 hours in total. Subsequently, the samples were heated at a rate of 200 °C/h to an artificial aging temperature of 185 °C and kept in the furnace for variable times (max. 24 h) before being quenched in water. Vickers hardness was measured for each aging time using a Struers DuraScan-70. The average hardness values were calculated based on 10 indentations with 5 kg force.

Slices were cut from the samples and polished down to a thickness of  $\approx 100 \mu\text{m}$ . Discs from these slices with a diameter of 3 mm were further electropolished to TEM specimens with a Struers TenuPol-5, using a solution of 1/3 nitric acid and 2/3 methanol. The applied voltage was 20 V at a temperature of  $-25 \text{ }^\circ\text{C}$ . Bright-field TEM images of the precipitate microstructure were acquired using a LaB<sub>6</sub> Philips CM30 operated at 150 kV. A post-column Gatan parallel electron energy loss spectroscopy (EELS) system was used to estimate the thickness of the specimen at the points where images were taken. The specimens were imaged in the  $\langle 001 \rangle_{\text{Al}}$  direction to enable measurement of precipitate length and cross-sectional area. The counting and measuring was conducted using an in-house algorithm. See [7] for

details regarding the quantification procedure. Elemental analysis was conducted using an Oxford INCA energy-dispersive X-ray spectroscope (EDS) on a Jeol JEM-2010F field emission gun microscope operated at 200 kV.

The hardness measurement samples were also prepared for SEM imaging. They were polished to a roughness of 1  $\mu\text{m}$  and further electropolished using a Struers Pollectrol with the “A2” electrolyte (70 % ethanol, 10 % 2-butoxyethanol, 8 % perchloric acid, 12 % distilled water). The voltage was set to 30 V and the polishing time to merely 1 second to prevent too much preferential etching of the Al matrix. A Jeol JSM-840 with a tungsten filament was used for imaging. In a SEM, the intensity of backscattered electrons is dependent on the average atomic number per volume (Z-contrast). We therefore used a backscattered electron detector to detect Ca-containing particles and separate them from Fe-containing particles. In addition, EDS analysis was conducted using a Hitachi TM3000 tabletop SEM. X-ray diffraction (XRD) was done on SEM samples using a Siemens D5005 instrument.

### **3. Results**

#### *3.1. Hardness evolution and microstructure*

The hardness evolution during artificial aging of the three alloys (Fig. 1) gives a rough overview of the precipitation kinetics. The overall shapes of the curves are conserved when Ca is added, but even small amounts (0.0060% = 60 ppm) of Ca cause a measurable decrease in peak hardness. It is interesting to note that Ca also decreases the hardness in samples which have only been stored for 4 hours at RT (no aging).

We selected the samples aged for 12 hours for TEM analysis as these

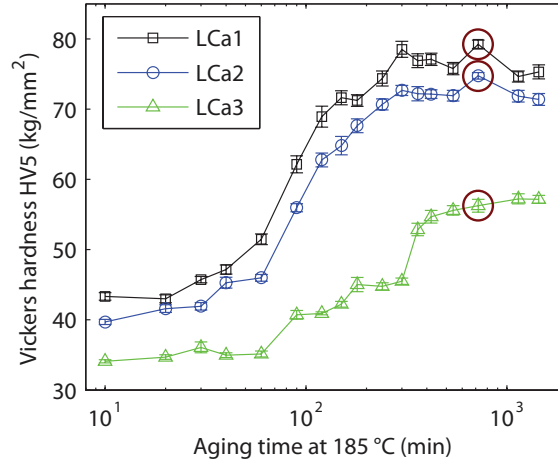


Figure 1: Vickers hardness of samples with compositions shown in Table 1 during artificial aging at 185 °C. The conditions selected for TEM analysis are marked with circles, and correspond to 12 h aging.

are roughly peak aged. Figure 2 shows an overview of the precipitate microstructure in this condition for each of the alloys. We take note of the following:

- The base alloy (LCa1) contains a homogenous microstructure of mostly  $\beta''$  precipitates.
- The microstructure in LCa3 is dominated by  $\beta'$  and  $B'$  precipitates, which is characteristic of overaged materials. When compared to LCa1, there are fewer precipitates, which on average are longer and have larger cross-sections. Some inhomogeneity exists: certain areas have higher precipitate number densities and a larger fraction of small  $\beta''$  precipitates (see Fig. 3(a) for an example).

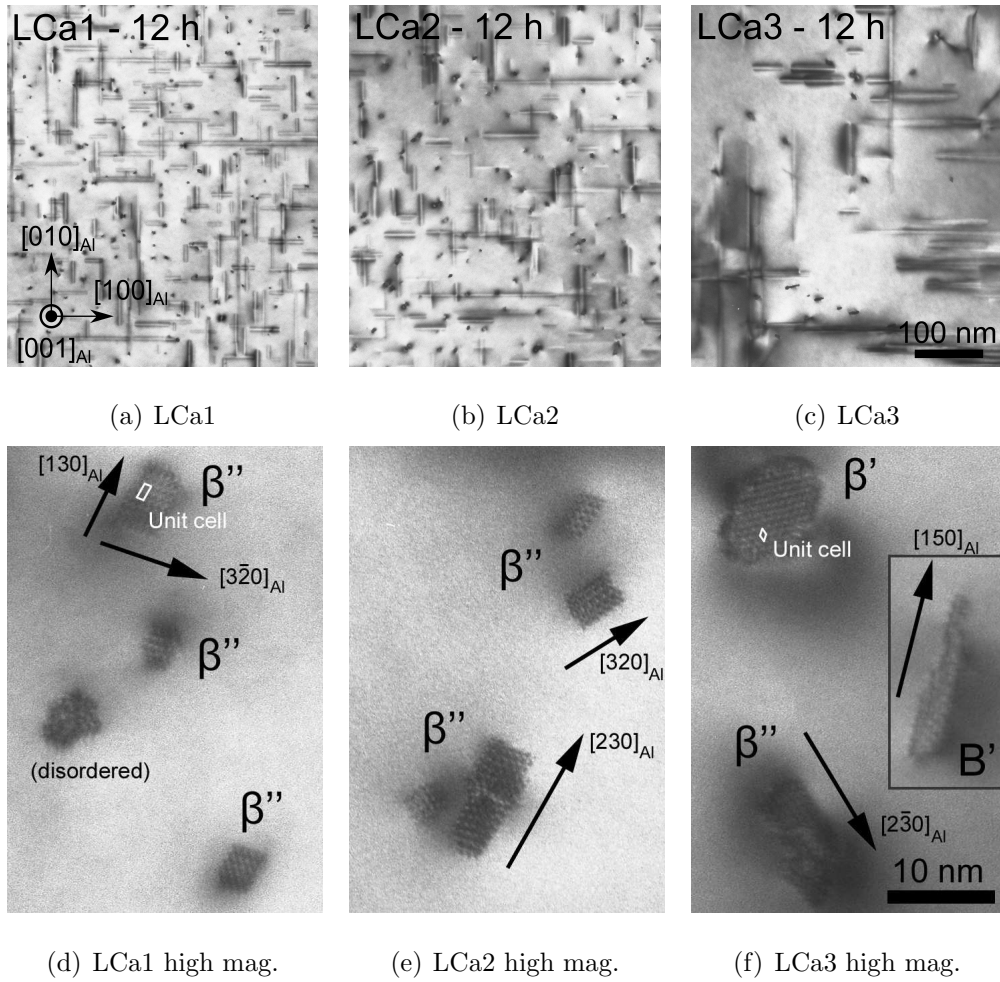
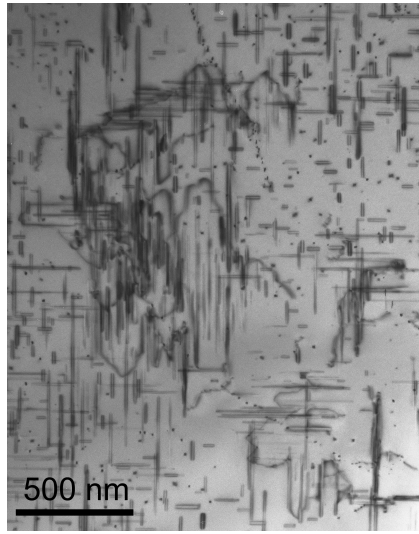


Figure 2: Bright-field TEM images of the microstructure in the three studied alloys, aged for 12 h at 185 °C. The viewing directions is along  $\langle 001 \rangle_{\text{Al}}$ , and the thickness of the specimens are in the range 90–150 nm. Images (d–f) show typical precipitate types in the three alloys.



(a) Inhomogeneity: The top right and lower left corners have a fine,  $\beta''$ -dominated microstructure, while we otherwise see a coarser mixture of  $\beta''$ ,  $\beta'$  and  $B'$ .



(b) A Ca-containing particle embedded in the Al matrix. Note the precipitate-free zone on the right side of the particle.

Figure 3: Low-magnification bright-field TEM images of the LCa3–12 h condition, both oriented in a direction close to  $\langle 001 \rangle_{\text{Al}}$ .

- LCa2 and LCa3 contain elongated,  $\mu\text{m}$ -sized particles (referred to in the further as Ca-containing particles). These always appear thick although in a thin area of the TEM samples, and were thus less etched by the electropolishing than the Al matrix. An example particle is shown in Fig. 3(b).
- The reduced number density of precipitates in LCa2, which has only 60 ppm of Ca, can already be visually distinguished from that of LCa1 in Fig. 2.

The Ca-containing particles are too large and form with a too low number density to be suitable for TEM investigations, apart from EDS analysis. SEM imaging and composition determination of the particles is presented in Section 3.2.

Based on bright-field TEM images as those in Fig. 2, the average precipitate morphology and number density were measured for the three alloys, and are shown in Table 2. As observed in Fig. 2, the addition of 0.07 at.% Ca has drastic effects, reducing the number density of precipitates by a factor of 8 and increasing their average volume by a factor of 6, resulting also in a smaller volume fraction.

### 3.2. Ca-containing particles

The large, elongated particles found in the LCa3–12 h condition by TEM were probed with EDS, and were found to contain Ca. Rounded iron-containing dispersoids of similar sizes were also found in all three alloys. EDS measurements of five particles gave the following quantified atomic fractions:  $(41.63 \pm 0.19)$  % Al,  $(39.80 \pm 0.48)$  % Si and  $(18.57 \pm 0.31)$  % Ca. An estimated thickness of 100 nm and the same density as pure Al were used in the

Table 2: Characterization of precipitate microstructure in the three alloys. The errors are all statistical except the error in specimen thickness, which is estimated to 10 %.

Condition	Cross-section [nm <sup>2</sup> ]	Length [nm]	Number density [ $10^3\mu\text{m}^{-3}$ ]	Volume fraction [%]
LCa1–12 h	$17.32 \pm 0.55$	$41.1 \pm 1.8$	$11.5 \pm 1.2$	$0.82 \pm 0.10$
LCa2–12 h	$22.68 \pm 0.86$	$58.5 \pm 2.8$	$6.38 \pm 0.68$	$0.85 \pm 0.10$
LCa3–12 h	$35.8 \pm 2.5$	$115 \pm 12$	$1.48 \pm 0.18$	$0.61 \pm 0.11$

quantification.

Attempts to unambiguously identify the phase of the particles have failed for the following reasons: Not being etched by the electrolyte, the particles were too thick for electron diffraction studies. An attempt was made to prepare a TEM sample using cold stage ion milling, but this removed or destroyed the Ca-containing particles while leaving Fe-containing phases intact. X-ray diffraction (XRD) of SEM samples was also attempted, with diffraction angles from  $2\theta = 5^\circ$  to  $120^\circ$  and a run time of 21 hours. The XRD spectrum showed Al and AlFe/Al<sub>3</sub>Fe phases, but no signs of any phase containing Ca. With such a small volume fraction and possibilities for unknown orientation relationships with the Al matrix, the particles are apparently very difficult to detect by XRD.

By comparing the size and distribution of Ca-containing particles in LCa3–12 h and LCa3–RT (no aging) in the SEM, we found that the particles did not change during artificial aging, and must have been fully developed during earlier high-temperature treatments associated with casting, homogenization, extrusion and solution heat treatment. Figure 4 displays the surface of the LCa3–10 min sample as viewed with backscattered electrons in a SEM. EDS maps were also obtained, showing the distribution of relevant elements close to the sample surface. The Ca-containing particles are plate-shaped, with a thickness of roughly 0.4  $\mu\text{m}$  and typical extent of 10  $\mu\text{m}$ . SEM images taken parallel to the extrusion direction enabled the measurement of the area fraction of the particles, which should be equal to their volume fraction. Measuring on images encompassing 422 particles, we found a volume fraction of  $(0.29 \pm 0.03)\%$  (statistical error) in LCa3–10 min.

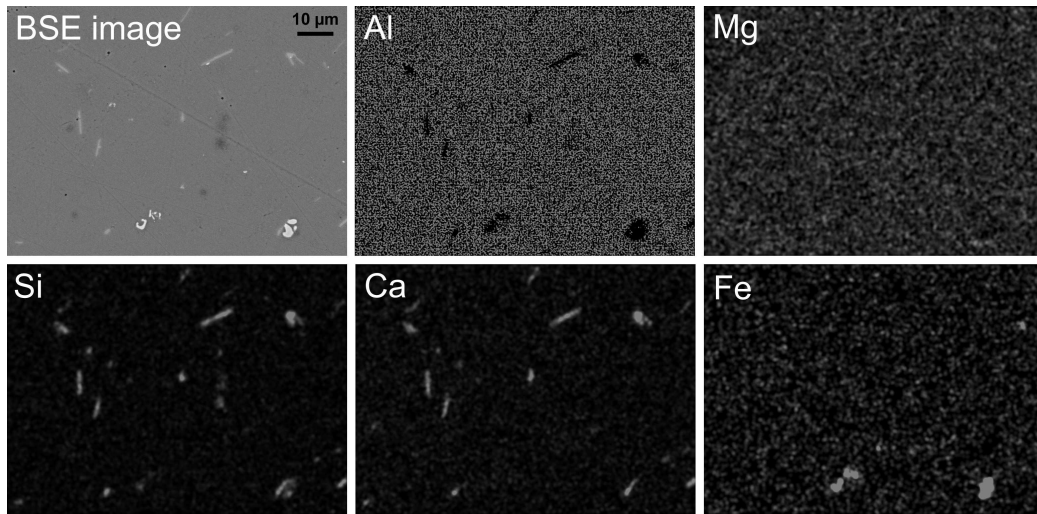


Figure 4: A backscattered electron SEM image of condition LCa3–10 min, with corresponding elemental EDS maps. The acceleration voltage was 15 kV. The viewing direction is parallel with the extrusion direction. Ca- (and Si-) containing plate-shaped particles are easily distinguished from iron-containing constituent particles and dispersoids based on shape and backscattered electron contrast.

A SEM sample with the extrusion direction perpendicular to the surface normal was also made. As shown in Fig. 5, the Ca-containing particles were found to be inhomogeneously distributed and oriented along the extrusion direction.

### 3.3. Presence of Ca elsewhere

In addition to using EDS measurements in a TEM to probe the large particles in the LCa3–12 h sample, we also checked its hardening precipitates for traces of Ca. Three  $\beta''$  and one B' were analyzed and did not contain measurable levels. See Fig. 6 for examples of EDS spectra from the precipitates, compared to a spectrum from a Ca-containing particle such as the one de-

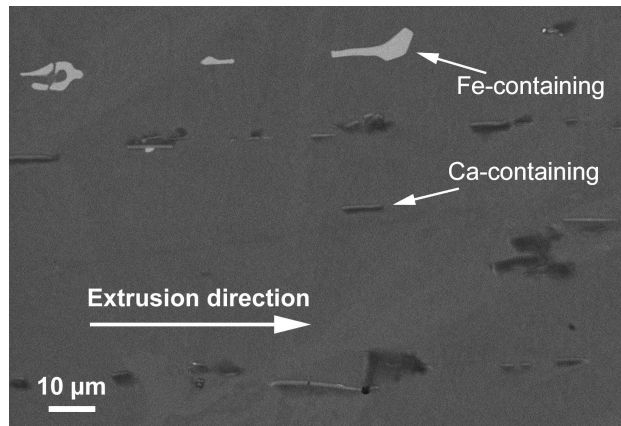
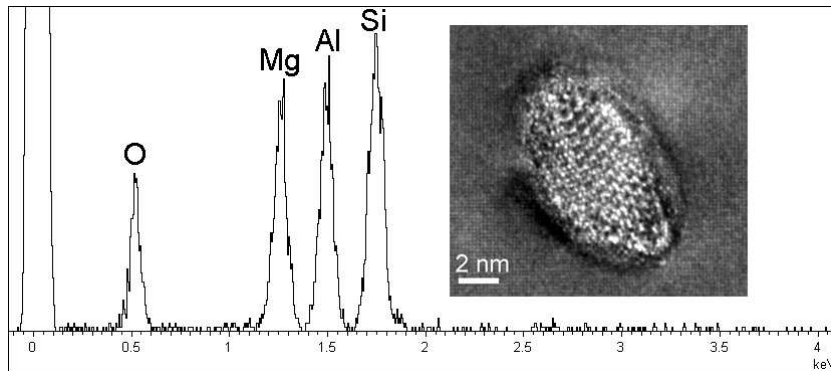
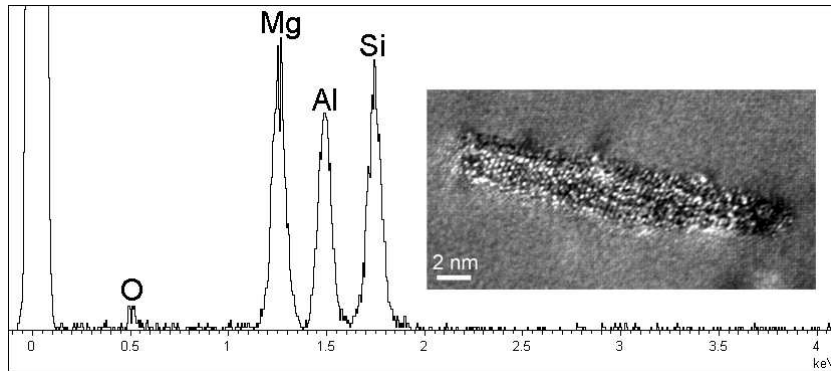


Figure 5: Backscattered electron image of sample with surface normal perpendicular to the extrusion direction (condition LCa3–20 min). The acceleration voltage was 10 kV. The Ca-containing particles are inhomogenously distributed in the Al matrix and were deformed during the extrusion of the material.

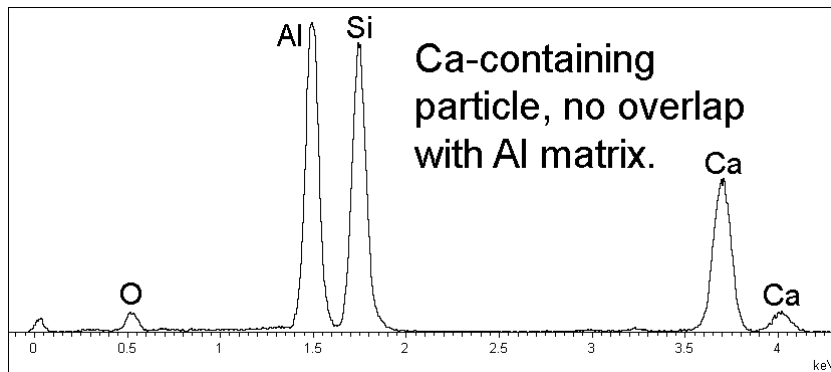
picted in Fig. 3(b). We also conducted an analytical scanning TEM (STEM) measurement with an EDS acquisition time of about 4 hours. Figure 7 shows the annular dark field (ADF) STEM image and elemental EDS maps. The image contains a low-angle grain boundary (GB) with GB precipitates, and hardening precipitates in two grains which are close to a  $\langle 001 \rangle_{\text{Al}}$  orientation. No segregation of Ca at the grain boundary or in the hardening precipitates is visible. The concentration of Ca estimated from the EDS map is 0.05 at.% in the whole image, which is around 70 % of the total Ca concentration in the material. The precipitates on the grain boundary are most likely Mg–Si phases which have been etched by the electrolyte during sample preparation and are now oxidized and Mg-poor.



(a) A partially disordered  $\beta''$ .



(b) A partially disordered  $B'$ .



(c) A Ca-containing particle.

Figure 6: EDS spectra acquired by TEM, with the electron beam focused on two hardening precipitates (respective images included) and one Ca-containing particle.

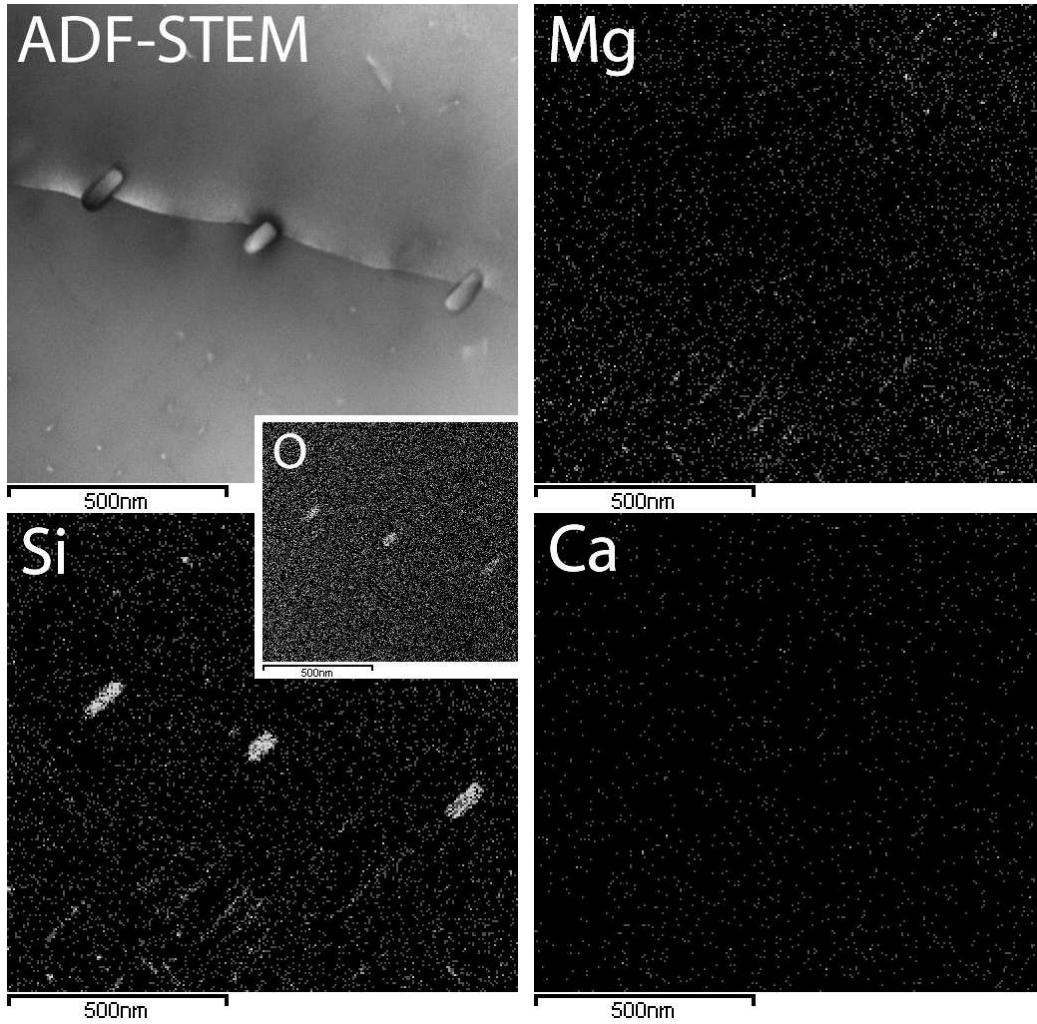


Figure 7: An annular dark-field scanning transmission electron microscopy image (ADF-STEM) and associated elemental energy-dispersive X-ray spectroscopy (EDS) maps, showing the concentration of the different elements around a grain boundary. Hardening precipitates are visible as needles along  $\langle 001 \rangle_{Al}$  directions in the upper and lower parts of the Mg and Si maps. No segregation of Ca is visible.

#### 4. Discussion

Figure 1 reveals that even 60 at.ppm Ca (LCa2) has a measurable negative influence on the hardness. Previous investigations [5] show no effect on yield strength in a similar alloy when 59 at.ppm Ca is added, suggesting that concentrations below these values have little influence in practical applications. It is clear from the precipitate quantification found in Table 2 that the hardness decrease with Ca additions is caused by a coarsening of the precipitate microstructure along with a change in precipitate types and a slight volume fraction decrease. The microstructure observed in LCa3–12 h contains more precipitates that are associated with overaging than that of LCa1–12 h, judging from the precipitation sequence in Eq. (1). The low hardness of LCa3 is produced by a mixture of  $\beta''$  precipitates (also found in LCa1 and LCa2) with  $\beta'$  and B' precipitates. Previous studies [8, 9] have shown that coarsening and apparent over-aging can be a consequence of a reduced solute content and/or an increased Mg/Si ratio in the alloy.

The Si content available in the solid solution must be reduced through the formation of Ca-containing particles. EDS measurements on the particles gave the approximate ratios Ca:Al:Si = 1:2:2. This fits with the stable phase  $\text{CaAl}_2\text{Si}_2$ , which has a hexagonal structure with lattice parameters  $a = 0.413$  nm,  $c = 0.7145$  nm, and space group  $P\bar{3}m1$  [10, 11]. As pointed out in [12], the phase is isostructural to the overaged U1– $\text{MgAl}_2\text{Si}_2$  phase in the Al–Mg–Si alloy system, with Mg replaced by Ca. This replacement expands the unit cell by 3.3 vol.%, which might make the phase incoherent with the Al lattice. In any case, the phase is seen grow as large particles, unaffected by typical aging temperatures, and is therefore probably stable

outside the Al matrix. It is unlikely that the particles have any hardening potential in Al. As explained in Sec. 3.2, we did not succeed in obtaining diffraction data (electron or X-ray) from the phase, and cannot confirm the U1–Ca structure. From the compositional measurements, this is still the most probable structure candidate for the observed phase. An inhomogeneous distribution of particles with composition  $\text{CaAl}_2\text{Si}_2$  have also been found in Al–Si foundry alloys with 185 at.ppm Ca additions [13].

Figure 5 shows that the process of extrusion aligns the particles parallel to the extrusion direction. From SEM quantification, the volume fraction of the particles was estimated to 0.29 % in the LCa3 samples. Using the number of Ca atoms per volume in the U1–Ca structure, we find that 61 % of the Ca is inside the large particles. This leaves 0.03 at.% Ca in solid solution, which seems reasonable given the EDS measurement of 0.05 at.% in the small area of Fig. 7. 23 % of the Si is also needed to form the U1–Ca particles, which increases the solid solution Mg/Si (atomic) ratio from 1.35 to 1.75. Al–Fe–Si phases (seen in Fig. 4) also require some Si to form, lowering the effective Si content even further. By comparison, the Mg/Si ratio has been measured to 1.1 in  $\beta''$  [14] (atom-probe tomography) and to 1.68 [15], 1.39 [16] and 1.69 [17] in  $\beta'$  (all with EDS). With an increasing solid solution Mg/Si ratio as a function of Ca content, we can explain why the precipitate types change as Ca is added. The explanation also makes the reason for the inhomogeneity in the microstructure of LCa3 apparent. Far from a Ca-containing particle, more Si is available in solid solution, and an island of fine microstructure can appear during aging. The amount of Si in the bulk could not be directly measured using EDS due to local accumulations (possibly of silicon oxide on

the TEM specimen surface).

## 5. Conclusions

We have measured the hardness evolution during artificial aging of a base Al–Mg–Si alloy with 0.0019, 0.0060 and 0.0727 at.% Ca additions and studied the materials using TEM and SEM. After 12 h aging at 185 °C, the peak Vickers hardness of the alloys were 79, 75 and 56, respectively. The hardness decrease with the addition of small quantities of Ca stresses the importance of impurity removal during production of Al alloys. From a fine, homogenous microstructure of  $\beta''$  needles, Ca additions cause a change to larger, less coherent  $\beta'$  and  $B'$  precipitates, lowering the mechanical strength. The change in microstructure is caused by a deficiency of Si. During casting, micrometer-sized particles with composition  $\text{CaAl}_2\text{Si}_2$  form and absorb nearby Si, leading to larger and less coherent precipitates and a more inhomogeneous microstructure. The large particles themselves are incoherent and have no hardening potential. Ca was not found to accumulate in hardening precipitates or along grain boundaries, but stays in solid solution if not included in the large particles.

## Acknowledgements

This work was financially supported by The Research Council of Norway and Norsk Hydro via project no. 193619, The Norwegian–Japanese Al–Mg–Si Alloy Precipitation Project.

- [1] J. R. Davis (Ed.), Aluminum and Aluminum Alloys, ASM Specialty Handbook, ASM International, 1993.

- [2] G. A. Edwards, K. Stiller, G. L. Dunlop, M. J. Couper, The composition of fine-scale precipitates in Al–Mg–Si alloys, *Mater. Sci. Forum* 217–222 (1996) 713–718.
- [3] K. Matsuda, Y. Sakaguchi, Y. Miyata, Y. Uetani, T. Sato, A. Kamio, S. Ikeno, Precipitation sequence of various kinds of metastable phases in Al–1.0mass% Mg<sub>2</sub>Si–0.4mass% Si alloy, *J. Mater. Sci.* 35 (2000) 179–189.
- [4] S. J. Andersen, C. D. Marioara, A. Frøseth, R. Vissers, H. W. Zandbergen, Crystal structure of the orthorhombic U2–Al<sub>4</sub>Mg<sub>4</sub>Si<sub>4</sub> precipitate in the Al–Mg–Si alloy system and its relation to the  $\beta'$  and  $\beta''$  phases, *Mater. Sci. Eng. A* 390 (2005) 127 – 138.
- [5] T. Furu, N. Telioui, C. Behrens, J. Hasenclever, P. Schaffer, Trace elements in aluminium alloys: Their origin and impact on processability and product properties, in: 12th International Conference on Aluminum Alloys, The Japan Institute of Light Metals, 2010.
- [6] R. Bjørge, C. D. Marioara, S. J. Andersen, R. Holmestad, Precipitation in two Al–Mg–Ge alloys, *Metallurgical and Materials Transactions A* 41 (2010) 1907–1916.
- [7] C. Marioara, H. Nordmark, S. Andersen, R. Holmestad, Post- $\beta''$  phases and their influence on microstructure and hardness in 6xxx Al–Mg–Si alloys, *Journal of Materials Science* 41 (2006) 471–478. 10.1007/s10853-005-2470-1.

- [8] C. D. Marioara, S. J. Andersen, H. Zandbergen, R. Holmestad, The influence of alloy composition on precipitates of the Al–Mg–Si system, *Metallurgical and Materials Transactions A* 36 (2005) 691–702. 10.1007/s11661-005-0185-1.
- [9] S. Wenner, C. D. Marioara, S. J. Andersen, R. Holmestad, Effect of room temperature storage time on precipitation in Al–Mg–Si(–Cu) alloys with different Mg/Si ratio, *Int. J. Mater. Res.* 103 (2012) 948–954.
- [10] E. Gladyshevskii, P. Kripyakevich, O. Bodak, Crystal structure of  $\text{CaAl}_2\text{Si}_2$  and analogous compounds, *Ukrain. Fiz. Zhur.* 12 (1967) 447–453.
- [11] Materials Science International Team, R. Schmid-Fetzer, Light Metal Systems. Part 1, volume 11A1 of *Landolt-Börnstein - Group IV Physical Chemistry*, Springer-Verlag, pp. 150–158.
- [12] S. Andersen, C. Marioara, R. Vissers, A. Frøseth, H. Zandbergen, The structural relation between precipitates in Al–Mg–Si alloys, the Al–matrix and diamond silicon, with emphasis on the trigonal phase  $\text{U1-MgAl}_2\text{Si}_2$ , *Materials Science and Engineering: A* 444 (2007) 157 – 169.
- [13] T. Ludwig, P. L. Schaffer, L. Arnberg, Influence of some trace elements on solidification path and microstructure of Al–Si foundry alloys, 2013. Submitted to *Metal. Trans. A*.
- [14] H. S. Hasting, A. G. Frøseth, S. J. Andersen, R. Vissers, J. C. Walmsley, C. D. Marioara, F. Danoix, W. Lefebvre, R. Holmestad, Composition of

- $\beta''$  precipitates in Al–Mg–Si alloys by atom probe tomography and first principles calculations, *J. Appl. Phys.* 106 (2009) 123527.
- [15] K. Matsuda, S. Tada, , S. Ikeno, in: T. H. Sanders, E. A. Starke (Eds.), *Proc. 4th Int. Conf. on Aluminum Alloys*, Georgia Institute of Technology, 1994, p. 605.
- [16] C. Cayron, P. A. Buffat, Transmission electron microscopy study of the  $\beta'$  phase (Al–Mg–Si alloys) and QC phase (Al–Cu–Mg–Si alloys): ordering mechanism and crystallographic structure, *Acta Materialia* 48 (2000) 2639 – 2653.
- [17] R. Vissers, M. A. van Huis, J. Jansen, H. W. Zandbergen, C. D. Marioara, S. J. Andersen, The crystal structure of the  $\beta'$  phase in Al–Mg–Si alloys, *Acta Materialia* 55 (2007) 3815–3823.